V European Conference on Computational Fluid Dynamics
ECCOMAS CFD 2010
J. C. F. Pereira and A. Sequeira (Eds)
Lisbon, Portugal,14-17 June 2010

MODELLING HAEMODYNAMICS IN PATIENT-SPECIFIC CAROTID BIFURCATIONS USING THE LOCALLY CONSERVATIVE GALERKIN (LCG) METHOD

Rhodri L. T. Bevan[†], Perumal Nithiarasu[†], Raoul Van Loon[†], Igor Sazonov[†] and Heyman Luckraz[††]

[†]Swansea University
Civil and Computational Engineering Centre, School of Engineering,
Swansea University, Swansea,SA2 8PP, United Kingdom
e-mail: P.Nithiarasu@Swansea.ac.uk
[††]Royal Wolverhampton Hospital
Heart and Lung Centre, Royal Wolverhampton Hospital, Wolverhampton, United Kingdom

Key words: carotid bifurcation, patient-specific modelling, LCG, local flux conservation, CBS, wall shear stress

Abstract. *Blood flow modelling within a carotid artery bifurcation is of interest with regards to the genesis and diagnosis of atherosclerotic plaques. In the present study, arterial geometry was reconstructed using AMIRA and an in-house meshing software. Boundary layer meshes were employed to accurately resolve high near-wall velocity gradients inside the artery.*

A locally conservative Galerkin (LCG) spatial discretisation was applied along with an artificial compressibility and characteristic based split (CBS) scheme to solve the 3D incompressible Navier-Stokes equations. The blood was modelled as a Newtonian fluid and a no-slip boundary condition was applied to the vessel wall. A Womersley profile was applied to the inflow and outflow boundaries.

Six haemodynamic wall parameters were brought together to analyse the regions of possible atherogenesis within the domain. The right carotid geometry from a healthy subject (Patient 1) was examined. The results show that wall shear stress (WSS) was high (6-15Pa) at the apex, along with a small region where WSS exceeded 20Pa. However, low WSS occurred in the common carotid artery (CCA). High oscillatory shear occurred in the CCA distal to a local narrowing of the internal carotid artery (ICA) and along the outer wall, indicating a potential region of atherogenesis. The highest values of wall shear stress angle deviation (WSSAD) and wall shear stress angle gradient (WSSAG) occur at the apex. The wall shear stress temporal gradient (WSSTG) reached 4000 Pa/s near the apex, closer to the ECA. Wall shear stress spatial gradient (WSSG) values corresponded with the WSS, with a maximum occurring at the apex.

Further patient-specific arterial geometries will be analysed during the presentation. These geometries are derived from patients that have been clinically diagnosed with a stenosis in a carotid artery.

1 INTRODUCTION

Clinical observations have shown that atherosclerotic disease typically occur at regions of complex haemodynamics such as arterial bifurcations or regions of high curvature. In the present work, patient-specific modelling of a carotid bifurcation is undertaken.

Current research has found that low or oscillatory wall shear stress is associated with atherogenesis [1–4] and high oscillatory shear stresses have been shown to induce inflammatory pro-atherogenesis effects such as monocyte adhesion [5,6]. In contrast, high shear stress has been shown to induce mechanical and/or chemical mechanisms that work in concert to provide athero-protective effects [7].

Bots *et al* [8] found that an increased carotid artery intima-media thickness (IMT) is an indicator of atherogenesis. Investigations [9] quantified the relationship between the IMT and several derived haemodynamic parameters for the common carotid artery (CCA).

Six haemodynamic wall parameters are brought together and investigated in this work. These are the time-averaged wall shear stress (WSS), time-averaged wall shear stress spatial gradient (WSSG), maximum wall shear stress temporal gradient (WSSTG), the oscillatory shear index (OSI), wall shear stress angle deviation (WSSAD) and wall shear stress angle gradient (WSSAG).

These parameters have been previously investigated by others, although none bring all of the parameters together. The OSI and WSSAD values were found to be reproducible over scans taken up to four weeks apart [2], although the WSS, WSSG and WSSTG values were not. The authors claim this was due to the significant dependence of the values on the mesh construction near the flow divider. The work of Hyun *et al* [10] investigated various design options for surgical reconstruction of diseased carotid bifurcations. The OSI and WSSAG were utilised to weigh the merits of each option. In another work [11] WSSTG and WSS were positively correlated against the number of smooth muscle cells and interstitial collagen and negatively correlated against the number of lipids and macrophages. The OSI was also correlated against these four variables with the opposite correlations observed. Gay *et al* [12] utilised OSI, WSS and particle residence time to understand blood clot formation and its location within an idealised stenosed and stented carotid artery. The diseased and stented arteries were found to have a significantly higher and oscillatory wall shear stresses compared to a healthy geometry. In the work of Younis *et al* [13], three healthy carotids were examined using WSS, OSI and WSSTG on a rigid wall model. The effect of the rigid wall assumption was investigated on one of the carotids using FSI modelling. Comparison between the results showed that for low WSS values, the distribution was similar. For high values of WSS there was a modest variation of up to 25%. A greater variation occurred in the OSI distribution. However from [11], is it believed that the rigid wall assumption influence in diseased arteries is minimal and the assumption is reasonable for assessing the distribution of wall shear stress derived parameters.

Investigation of the derived parameters requires good boundary layer meshes to cap-

ture the high velocity gradient in the vicinity of the vessel wall. However, only one of the papers previously mentioned has used any sort of boundary refinement. Therefore in the current work we bring together the six haemodynamic wall parameters for a thorough investigation of a patient-specific carotid bifurcation and introduce boundary layer refinement to provide sufficient detail in the near-wall region.

The locally conservative Galerkin (LCG) method is used as part of the computational analysis as a means of providing a rapid and parallelised solver. The method possesses the highly prized property of both finite volume methods and discontinuous Galerkin (DG) finite element methods, namely local conservation. Explicit local conservation of Galerkin finite element method has of only recently been implemented [14–18]. This method is both locally and globally conservative, endowing the method with advantages such as local hp-refinement and weak enforceability of the Dirichlet boundary conditions. The LCG method can avoid the drawbacks of the DG methods in two ways. In LCG, the multiple solutions at a node are averaged to produce a continuous solution for every time step, which reduces the memory requirements. The second part involves, instead of solving for extra variables, only a small post-processing calculation is used to find the interface fluxes. The LCG scheme outlined in the paper will give a solution equal to, or in some cases a more accurate solution, than standard Galerkin method due to its unconditional local and global conservation properties. The reason is due to the standard or global Galerkin method only being globally conservative if Neumann boundary conditions are used [19].

2 GOVERNING EQUATIONS AND THE CHARACTERISTIC BASED SPLIT(CBS) SCHEME

2.1 The artificial compressibility based Navier-Stokes equations

The equations may be written as
Continuity

$$\frac{1}{\beta^2}\frac{\partial p}{\partial t} + \rho\frac{\partial u_i}{\partial x_i} = 0 \tag{1}$$

Momentum

$$\frac{\partial u_i}{\partial t} + u_j\frac{\partial u_i}{\partial x_j} + \frac{1}{\rho}\frac{\partial p}{\partial x_i} - \frac{1}{\rho}\frac{\partial \tau_{ij}}{\partial x_j} = 0 \tag{2}$$

where u_i are the cartesian components of the velocity vector, ρ is the fluid density, p represents the pressure and β is an artificial compressibility parameter [20–22]. The deviatoric stress components τ_{ij} are related to the velocity gradients by

$$\tau_{ij} = \mu\left(\frac{\partial u_i}{\partial x_j} + \frac{\partial u_j}{\partial x_i} - \frac{2}{3}\frac{\partial u_k}{\partial x_k}\delta_{ij}\right) \tag{3}$$

Non-dimensional forms of the equations are used, along with appropriate reference quantities [20]. The problem definition is completed by selecting appropriate initial and boundary conditions.

2.2 Semi-discrete form of the characteristic based split (CBS) scheme

The characteristic based split (CBS) scheme is a well established algorithm in the continuous (or global) Galerkin context, for both incompressible and compressible flow simulations [21, 23–25]. The artificial compressibility form has been incorporated into the CBS family since 2003 [20, 22, 26].

The present work couples the semi-discrete CBS scheme with the LCG spatial discretisation procedure to obtain an element-wise solution strategy. The CBS approach adopted in this work, starts with a solution to an intermediate velocity field. This intermediate velocity field is then corrected, once the pressure field is obtained from a pressure (continuity) equation.

The three steps are defined (non-dimensional form) as:

1. Solve for the intermediate velocity field, ${u_i}^\dagger$

$$\frac{{u_i}^\dagger - {u_i}^n}{\Delta t} = -\left(\frac{\partial u_j u_i}{\partial x_j}\right)^n + \frac{\partial}{\partial x_j}\left(\frac{1}{Re}\frac{\partial u_i}{\partial x_j}\right)^n + \frac{\Delta t}{2}u_k\frac{\partial}{\partial x_k}\left(\frac{\partial u_j u_i}{\partial x_j}\right)^n \tag{4}$$

2. Solve for the pressure field, p^{n+1}

$$\frac{1}{\beta^2}\frac{p^{n+1}-p^n}{\Delta t} = -\rho\frac{\partial}{\partial x_i}\left({u_i}^\dagger - \Delta t\left(\frac{\partial p}{\partial x_i}\right)^n\right) \tag{5}$$

3. Solve for the corrected velocity field, ${u_i}^{n+1}$

$${u_i}^{n+1} = {u_i}^\dagger - \Delta t\left(\frac{\partial p}{\partial x_i}\right)^n + \frac{\Delta t^2}{2}u_k\frac{\partial}{\partial x_k}\left(\frac{\partial p}{\partial x_i}\right)^n \tag{6}$$

The value of β is determined locally, based on both convective and diffusive time-step restrictions [20, 21, 27]. Local determination makes the scheme suitable for different flow regimes (convection and diffusion dominated) within a problem at a particular Reynolds number. In this work the relation $\beta = \max(\epsilon, \nu_{conv}, \nu_{diff})$ is employed. The constant ϵ ensures that β does not approach zero, and typically takes the value of $0.1 \leq \epsilon \leq 0.5$. ν_{conv} is the local convective velocity and ν_{diff} is the local diffusive velocity. These velocities are calculated from the non-dimensional relations [20],

$$\nu_{conv} = \sqrt{u_i u_i} \qquad \nu_{diff} = \frac{1}{hRe} \tag{7}$$

Local time-stepping [21] is employed as an iteration mechanism to accelerate convergence to a solution and provide optimal stabilisation. A dual time-stepping approach is used to recover the transient solution [20, 25]. Steady state has been achieved when the L_2 residual norm of the velocity has reduced to 10^{-5}.

3 LCG SPATIAL DISCRETISATION

In this section, Equations (4), (5) and (6) are discretised in space using the locally conservative Galerkin (LCG) finite element method [14, 16–18]. The variation of each of the variables is approximated by the standard finite element spatial discretisation as $u_i \approx \tilde{u_i} = \mathbf{N}\mathbf{u_i}$ and $p \approx \tilde{p} = \mathbf{N}\mathbf{p}$ where $\mathbf{N}$ are the shape functions. In an LCG discretisation, the domain can be broken into elemental subdomains, thanks to the post-processed flux, if required. Following integration by parts and introduction of the Galerkin weighting, the final matrix form of the first step becomes

$$\{\mathbf{u_i}\}^{\dagger} = \{\mathbf{u_i}\}^n + [\mathbf{M1_e}]^{-1}\Delta t \left([\mathbf{K1_e}]\{\mathbf{u_i}\} + [\mathbf{K1_e^{cg}}]\{\mathbf{u_i}\} + \{\mathbf{f\hat{1}_e}\} \right)^n \tag{8}$$

Third order and higher terms are neglected. In the LCG method, the boundary terms are replaced with a numerical flux, $\hat{\tilde{F}}_{ij}$ and $\frac{\partial \hat{\tilde{F}}_{ij}}{\partial x_j}$, calculated at time (n) on the element boundaries. The final matrix form of the second step is

$$\{\mathbf{p}\}^{n+1} = \{\mathbf{p}\}^n + [\mathbf{M2_e}]^{-1}\Delta t \left([\mathbf{C2_e}]\{\mathbf{u_i}^{\dagger}\} - \Delta t[\mathbf{K2_e}]\{\mathbf{p}\}^n + \{\mathbf{f\hat{2}_e}\} \right) \tag{9}$$

and the third step is given by

$$\{\mathbf{u_i}\}^{n+1} = \{\mathbf{u_i}\}^{\dagger} + [\mathbf{M3_e}]^{-1}\Delta t \left([\mathbf{K3_e}]\{\mathbf{p}\} - [\mathbf{K3_e^{cg}}]\{\mathbf{p}\} + \{\mathbf{f\hat{3}_e}\} \right)^n \tag{10}$$

For a detailed description of the matrix form, the reader is referred to [17].

3.1 Calculation of face fluxes

To satisfy local conservation, the flux crossing a common face shared by two elements is made equal and forced to act in opposing directions (Figure 1).

$$F_{e1}n_{e1} + F_{e2}n_{e2} = 0 \tag{11}$$

where $F_{e1} = F_{e2}$ and n_{e1} and n_{e2} are the outward normals from the edges of the respective elements.

In order to enforce this condition, a small post-processing calculation is undertaken at the end of each time-step. This is possible once a solution is recovered from the previous time-step. The post-processing calculation uses the nodal values of the solution and its gradients, to provide an accurate interface flux. It is this flux that establishes connectivity between elements at the next time-step. For linear tetrahedral finite elements, the gradient

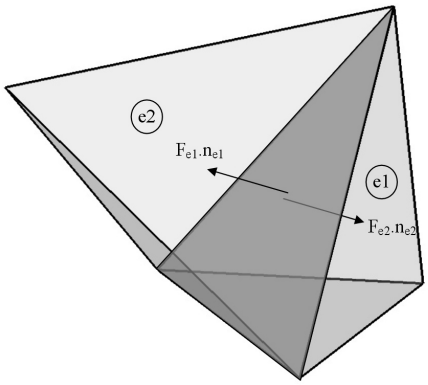

Figure 1: Flux crossing a common face between two tetrahedral elements

of the scalar variable is a constant within each element. A nodal approximation of the variable's gradient is computed by taking the mean of the connected element gradients.

3.2 Correction Factor for LCG Equation

At an internal node, in principle the equal and opposite fluxes introduced at the interfaces of the elements will cancel each other when the solution is averaged over a node. The only difference between the GG and the LCG equations described here lies thus in the use of the mass matrix. To ensure that the transient LCG method converges to the identical solution provided by the global Galerkin method, a correction factor based upon this difference must be implemented [17, 18]. The correction factor can be determined at a preprocessing stage for cases involving the Eulerian form of reference.

4 MESH GEOMETRY RECOVERY AND CONSTRUCTION

Geometry was constructed from sets of CT images. The healthy right carotid from Patient 1 was constructed from a set of scans provided by Singleton Hospital, Swansea, UK. The set consisted of 390 axial slices from the thorax to the nasal passage. Scan resolution was 0.877×0.877mm in the slice plane and 1mm between the slices. Further carotid geometries (left and right from each patient) were constructed from sets provided by Royal Wolverhampton Hospital, Wolverhampton, UK. Scan resolution was 0.35×0.35mm in the slice plane and 0.5mm between the slices. The sets consisted of approximately 500-600 slices. At least one of the carotids in each of the Wolverhampton sets has been clinically diagnosed with a stenosis.

The geometric reconstruction was undertaken using AMIRA. In order to improve the quality of the AMIRA surface mesh, surface coarsening and smoothing using the technique given by Saksono *et al* [28] was undertaken. Preparation of the surface mesh included introducing cuts to ensure the inlet and outlets were perpendicular relative to the arterial wall.

The wall shear stress derived parameters investigated need a high resolution meshing scheme along the vessel wall in order to capture the high velocity gradient close to the wall. Therefore, boundary layers are constructed by projecting the surface points inward along the surface normal. A new surface mesh is constructed from these new points, with the same topology as the outer surface mesh. The two surface meshes are connected together, first forming prisms, which are then subdivided into tetrahedra. Multiple boundary layers can be constructed through repetition of this technique. The volume mesh for the remainder of the domain is formed using a meshing solver based on the Delaunay method [29].

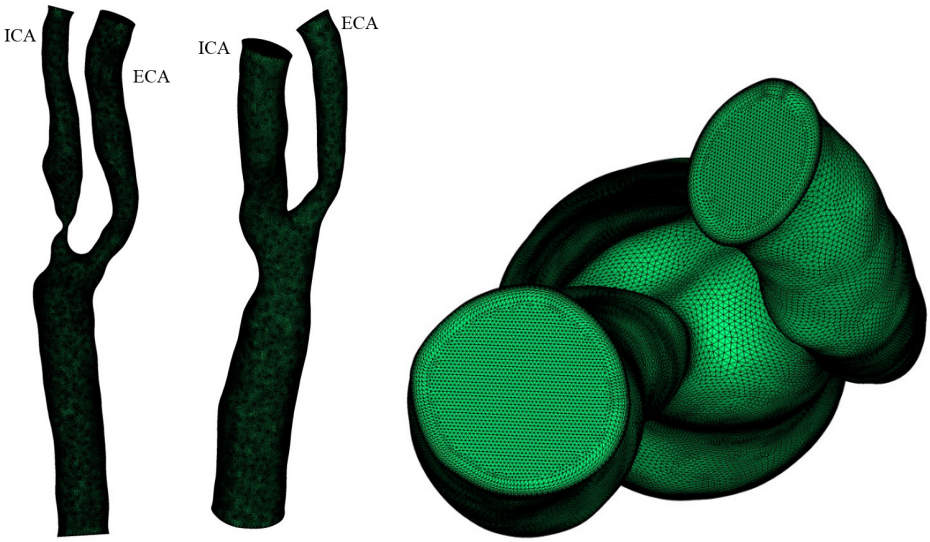

Figure 2: (a)Patient 2 Left and Right Carotid Meshes (b) Patient 2 Right Carotid with boundary layers.

Figure 2(a) illustrates the three arteries, the Internal Carotid Artery (ICA), the External Carotid Artery (ECA) and the Common Carotid Artery (CCA) for Patient 2 and demonstrates the flexibility of the boundary layer technique to deal with severe stenosis. The boundary layer mesh thickness exponentially decreases closer to the vessel wall. This thickness distribution were determined by the method outlined in [18, 28].

4.1 Boundary conditions

The blood dynamic viscosity and density are taken to be $\mu = 0.0035$ kg/m s and $\rho = 1.0 \times 10^3$ kg/m^3 respectively. A no-slip boundary condition was applied to the vessel wall. The blood flow is assumed to be unsteady and fully developed with a Womersley profile [2, 13, 30–33] being employed. Another alternative would be to use measured velocity profiles captured using MRI and phase contrast measurements. However, this was not possible in this case and thus a Womersley profile is used. Construction of the velocity profile, the harmonics used in waveform generation and the mapping procedure to map

the the flow profile to a non-circular cross section can be found in [18, 34].

The flow rate ratios at the outlets (ICA and ECA) vary in the literature from constant to non-uniform ratios in time [4, 35, 36]. Milner *et al* [35] concludes that while flow differences do play a role, geometry is the key influence. Therefore in order to simplify the boundary conditions, we have assumed an ICA flow rate of 60% and an ECA flow rate 40% of the total CCA flow rate for healthy geometries. Flow rates for the arteries containing a stenosis are adjusted to provide solutions that correspond to known instantaneous velocities proximal to the stenosis.

4.2 Convergence

Mesh convergence was undertaken on the right carotid from patient 1. Ten meshes were analysed, nine containing boundary layers (3-9,11,12 boundary layers respectively) and one without. The number of elements within the carotid mesh ranged from 1,465,562 linear tetrahedral elements purely unstructured mesh to 2,453,723 elements in the 12 boundary layered mesh. Convergence was taken to have occurred when the error is less than 1% between two consecutive meshes. The relative convergence error (Equation 12) is determined using the time-averaged wall shear stress (τ_{mean}) as defined in Section 5.1.

$$\text{error} = \frac{\max\left(\tau_{mean}\right)_i - \max\left(\tau_{mean}\right)_j}{\max\left(\tau_{mean}\right)_i} \tag{12}$$

The subscripts i and j refer to mesh i and j respectively. The convergence error between the eleven and twelve boundary layer meshes was less than 0.5% and between mesh with six and twelve layers, the error is about 8%. To obtain the best accuracy, the mesh with twelve layers consisting of 421,608 nodal points and 2,453,723 linear tetrahedral elements was selected. A time sensitivity analysis utilising 60,120 and 240 time steps for a cardiac cycle was also undertaken. Utilising Equation 12, with i and j denoting different time discretisations on the 12 layered mesh, the error was found to be less than 1% between the 60 and 120 time step discretisations. Therefore, the 120 time discretisations were assumed to be sufficient.

5 RESULTS

The results for the right carotid geometry from a healthy subject (Patient 1) are outlined in this section. Results for further patient-specific carotid geometries will be examined during the presentation.

5.1 Wall Shear Stress

Established research has shown that low wall shear stress is one of the indicators to the location of atherosclerotic plaque formation. To calculate the wall shear stress, the traction vector $\mathbf{t}$ is calculated from the Cauchy stress tensor $\boldsymbol{\sigma}$ and the surface normal vector $\mathbf{n}$ using Equation 13. The surface traction vector $\mathbf{t_s}$ can then be determined using

Equation 14. Finally, the HWP time-averaged wall shear stress (WSS), τ_{mean}, is calculated as the magnitude of the time-averaged surface traction vector (Equation 15).

$$\mathbf{t} = \boldsymbol{\sigma} \cdot \mathbf{n} \tag{13}$$

$$\mathbf{t_s} = \mathbf{t} - (\mathbf{t} \cdot \mathbf{n})\mathbf{n} \tag{14}$$

where $\|\cdot\|$ denotes the magnitude of the vector and T is the period of one cycle.

$$\tau_{mean} = \left\| \frac{1}{T} \int_0^T \mathbf{t_s} dt \right\| \tag{15}$$

The WSS distribution is shown for the right carotid of Patient 1 (Pat01R) in Figure 3. When the value of WSS is less than 0.5Pa, it is believed stimulation of an atherogenic phenotype occurs [37]. The majority of the CCA experiences less than 0.5 Pa which would indicate a possible region of atherogenesis, this is in good agreement with the work of Papathanasopoulou *et al* [3] which found low WSS in the carotid bulb. There are also small regions in the ICA and the ECA with a WSS value less than 0.5 Pa, and a significantly larger region with a value less than 1.0 Pa. Atherosclerotic plaque composition, according to Cheng *et al* [38], is dependent on whether the lesion experienced low shear stress or oscillating shear stress. The low shear stress plaque composition contained more "destabilising" components such as lipids and macrophages.

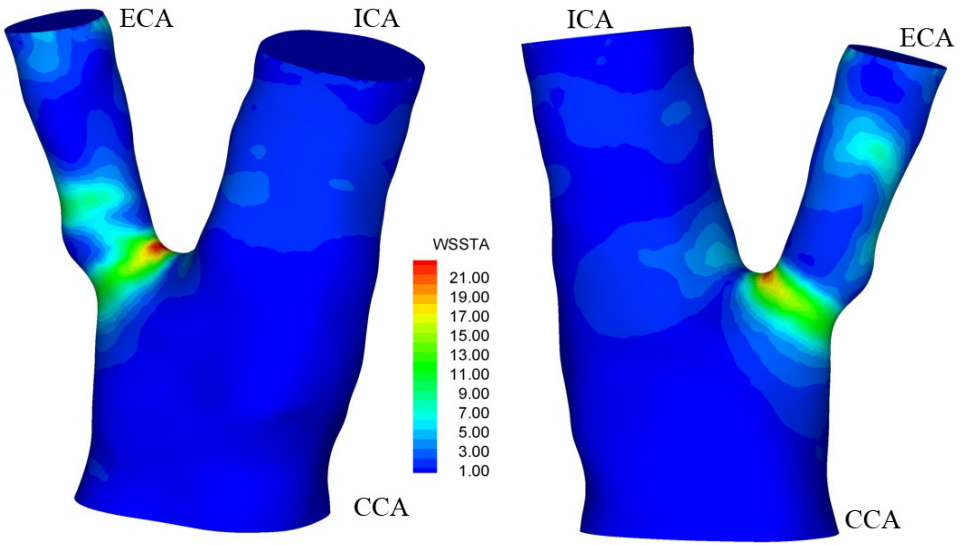

Figure 3: Pat01R. Time-averaged Wall Shear Stress (Pa) distribution within the carotid bifurcation (a) Posterior (b) Anterior

The highest values of WSS occur near the apex, experiencing values between 6-15Pa. A small region experiences a maximum peak time-averaged WSS of 23Pa. This region is

closer to the inner wall of the ECA which is in agreement with the results of Younis *et al* [13], who examined three patient-specific geometries and found this region experienced values of between 6-10Pa with a small region experiencing values over 10Pa.

5.2 Wall Shear Stress Spatial Gradient

The aim of the time-averaged wall shear stress spatial gradient (WSSG) is to identify the areas of locally disturbed flow. It is defined as [39]

$$\text{WSSG} = \frac{1}{T}\int_0^T \sqrt{\left(\frac{\partial \tau_x}{\partial x}\right)^2 + \left(\frac{\partial \tau_y}{\partial y}\right)^2 + \left(\frac{\partial \tau_z}{\partial z}\right)^2}\, dt \tag{16}$$

where τ_x is the x-coordinate component of the instantaneous shear stress vector $\mathbf{t_s}$. Since both positive and negative gradients contribute to atherosclerotic plaque formation [40, 41], an absolute value of the instantaneous WSSG is utilised. High WSSG values have been found to be indicative of decreased IMT thickness by Vermeersch *et al* [9]. These high values equate to sustained acceleration or deceleration within the flow. It can be seen from Figure 4 that the distribution of the WSSG is in good agreement with WSS, displaying peak values in a region near the flow divider and closer to the ECA. This indicates a potential athero-protected region whilst low WSSG values occur in the CCA and ICA.

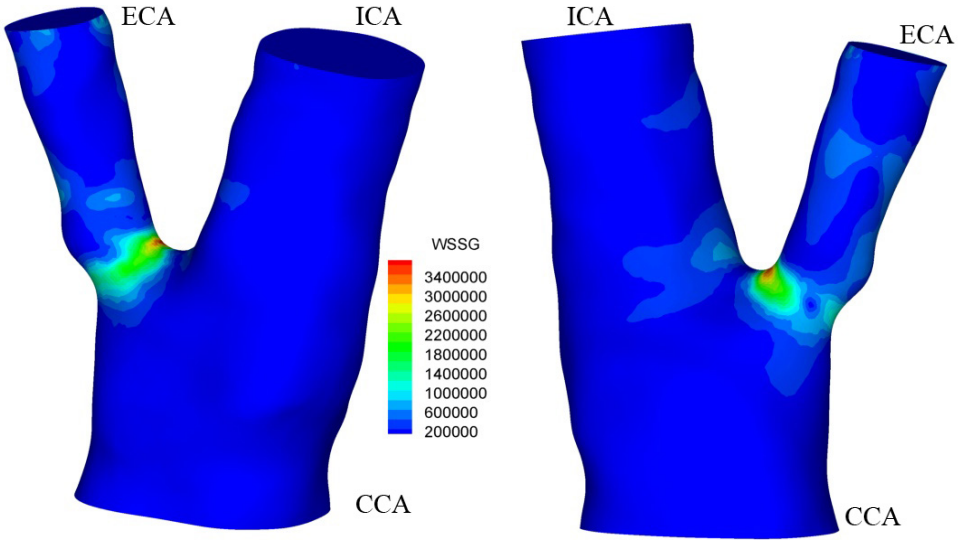

Figure 4: Pat01R. WSSG (Pa/m) distribution within the carotid bifurcation (a) Posterior (b) Anterior

5.3 Wall Shear Stress Temporal Gradient

The WSSTG was determined by calculating the temporal gradient between instantaneous wall shear stresses for every consecutive time step and keeping the maximum result,

as outlined in Equation 17.

$$WSSTG_i = \max\left(\frac{\partial \left\|\mathbf{t_s}\right\|_i}{\partial t}\right) = \max\left(\frac{\left\|\mathbf{t_s}\right\|_i^{n+1} - \left\|\mathbf{t_s}\right\|_i^{n}}{\Delta t}\right) \tag{17}$$

where i is the spatial point in question and $0 < t < T$. From Figure 5, it is possible to see that low values of WSSTG occur in the CCA, where it does not exceed 250 Pa/s and 350 Pa/s for all but a small area of the ICA. Peak values occur near the flow divider and close to the ECA, with values in excess of 4000 Pa/s, thus indicating an athero-protected region. The WSSTG distribution is in good agreement with WSS and WSSG. The predicted values of WSSTG also compare favourably to the work of Younis *et al* [13] and Kaazempur-Mofrad *et al* [11]. In the latter work, close correlation between the WSS and WSSTG was observed, although not in all of the four cases examined.

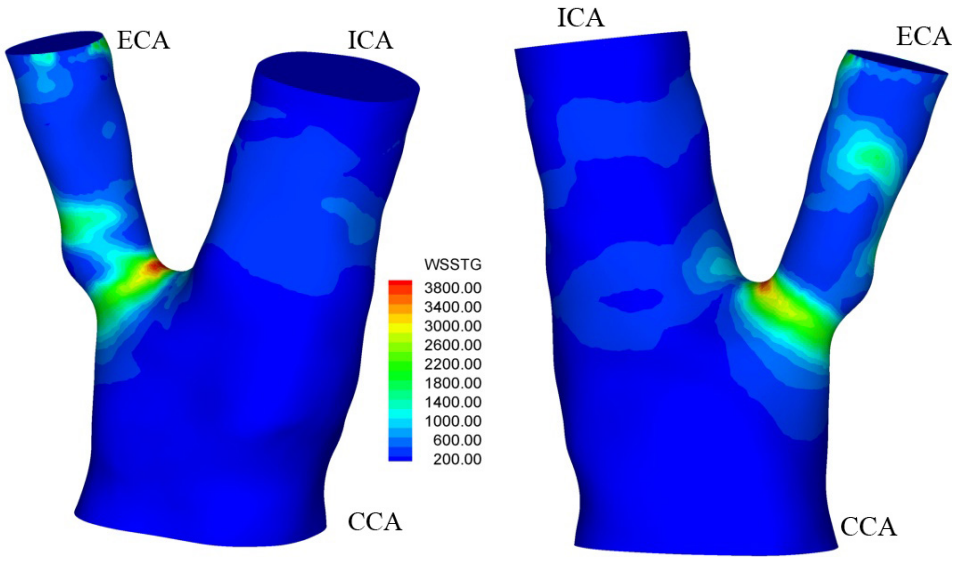

Figure 5: Pat01R. WSSTG (Pa/s) distribution within the carotid bifurcation (a) Posterior (b) Anterior

5.4 Oscillating Shear Index

The oscillatory shear index (OSI) [1, 42] is used to quantify the transient shear stress dynamics experienced by the endothelial cells. Tardy *et al* [43] determined that there is a correlation between the oscillating shear stress and the predisposition of lesion development. OSI is a ratio of the time-averaged wall shear stress and the absolute wall shear stress (τ_{abs}) given by

$$OSI = \frac{1}{2}\left(1 - \frac{\tau_{mean}}{\tau_{abs}}\right) \tag{18}$$

where

$$\tau_{abs} = \frac{1}{T}\int_0^T \|\mathbf{t_s}\|\, dt \tag{19}$$

The index will always lie within the range $0 \leq OSI \leq 0.5$. It does not take into account the magnitude of the shear stress vectors, only the vector directions. The parameter attempts to quantify the amount of time a point experiences flow away from the predominant axial direction within a cycle. The higher the value of the OSI, the greater the variation in shear stress direction over the time period in question.

OSI distribution within the carotid is shown in Figure 6. It can be seen that a region within the CCA displays a high OSI value, thus indicating a region of potential atherosclerotic plaque formation. This region is furthest from a local narrowing of the CCA and along the outer wall. This is in close agreement with the work of Kaazempur-Mofrad *et al* [11]. Several smaller regions occur in the ECA. There is also a region of elevated OSI extending from the apex along the wall of the CCA, although only a small section of the region contains significantly elevated values. and one occurs below the apex on the CCA wall. All the regions displaying high OSI values correspond to regions of low WSS.

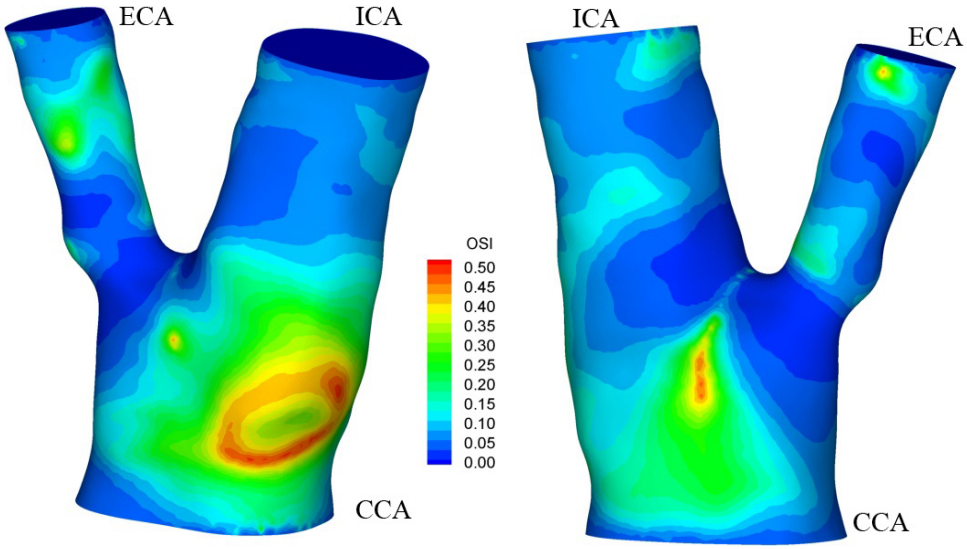

Figure 6: Pat01R. Oscillating Shear Index distribution within the carotid bifurcation (a) Posterior (b) Anterior

5.5 Wall Shear Stress Angle Deviation

The wall shear stress angle deviation (WSSAD) parameter is used to represent the spatial variation of the mean shear stress direction. It is defined [41] in Equation 20 and ϕ_i is defined in Equation 21. It can only be employed if the mesh nodes are approximately equidistant.

$$\text{WSSAD} = \frac{1}{T}\int_0^T \left(\frac{1}{A_i}\int_S \phi_i dA_i\right) dt \tag{20}$$

$$\phi_i = \arccos\left(\frac{\boldsymbol{\tau}_i \cdot \boldsymbol{\tau}_j}{\|\boldsymbol{\tau}_i\| \cdot \|\boldsymbol{\tau}_j\|}\right) \tag{21}$$

where A_i represents the sum of the connected element areas for node i, $\boldsymbol{\tau}_i$ denotes the surface stress vector at node i and $\boldsymbol{\tau}_j$ represents the surrounding surface stress vectors. $j = 1 : n$ where n is the number of connected points to node i.

From Figure 7, the peak values of the WSSAD occur at the flow divider and extend along the wall of the CCA. This region of high WSSAD approaches but does not overlap with the small region of significantly elevated OSI values near the apex. Away from the flow divider, elevated values of WSSAD occur within the high OSI region, although these values are markedly weaker than near the apex. At the inlet and outlets, the values of WSSAD are the result of imposing the velocity profiles and are ignored.

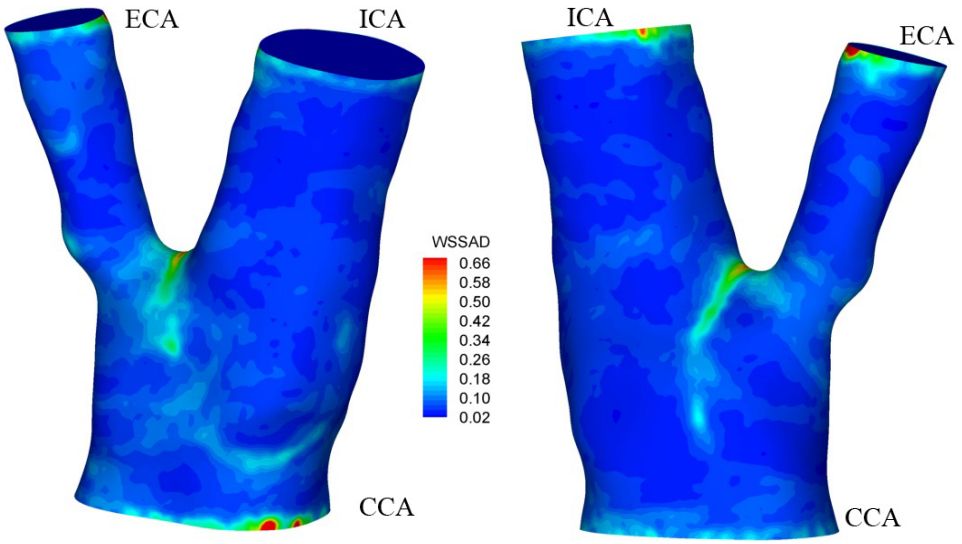

Figure 7: Pat01R. WSSAD (rad) distribution within the carotid bifurcation (a) Posterior (b) Anterior

5.6 Wall Shear Stress Angle Gradient

$$\text{WSSAG} = \frac{1}{T}\int_0^T \left|\frac{1}{A_i}\int_S \nabla\phi_i dA_i\right| dt \tag{22}$$

Time-averaged magnitude WSSAG values are shown in Figure 8. The parameter (Equation 22) is utilised as a mesh independent wall shear stress directional parameter [41]. It is time-averaged in order to identify locally high values of WSSAG which are

maintained throughout the cycle. Literature [9, 10], has established that high WSSAG can be an indicator of atherogenesis.

It can be seen from the distribution of WSSAG that a region of high WSSAG occurs at the flow divider, which is in good agreement with [39]. The elevated values of WSSAG extending away from the flow divider along the wall of the CCA are in good agreement with [10]. The peaks at the entrance and exits are the results of imposing the velocity profiles and they are ignored here.

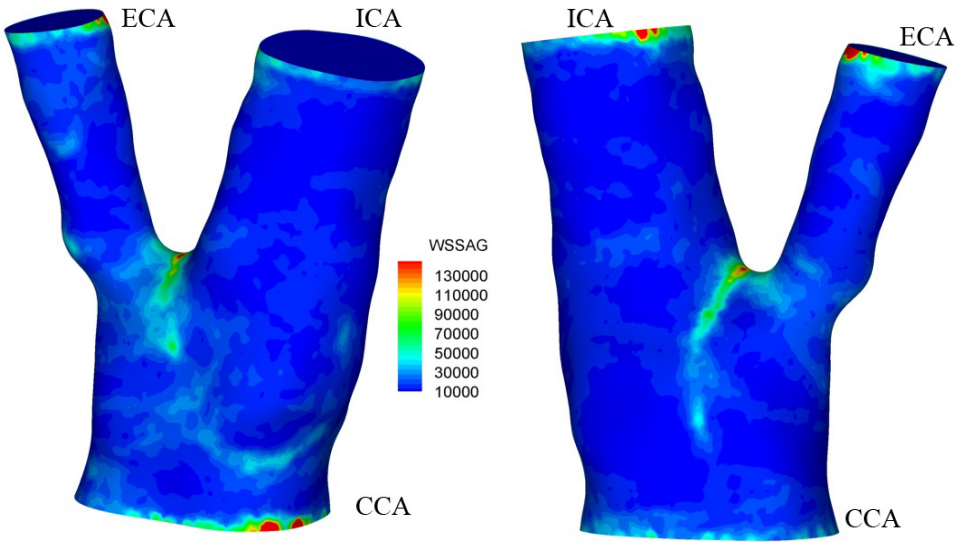

Figure 8: Pat01R. WSSAG (rad/m) distribution within the carotid bifurcation (a) Posterior (b) Anterior

6 Discussions

Six wall shear stress derived parameters have been brought together in order to assess their reliability in predicting potential atherosclerosis. Examining the parameters, it is necessary not only to look at any individual indicator, but also the combined assessment. It should also be noted that the results in the previous section deal with a healthy carotid bifurcation, which would perhaps tend to mask any clear signal indicating potential atherosclerosis.

It has been previously established that high values of OSI, WSSAD and WSSAG are indicative of regions of atherosclerotic plaque formation. Looking at the distribution of the OSI, it is possible to see that a region of potential atherogenesis exists in the CCA. The WSSAD and WSSAG parameters do show elevated values for this region, although they exhibit a stronger elevation in regions near the apex which correspond to low values of OSI.

Examining the distributions of the time-averaged wall shear stress along with the WSSG and WSSTG, it appears that low values predominate throughout the CCA, which

is a potential indicator for increased IMT. The high values of these parameters also indicate an athero-protected region close to the flow divider where a peak of 23Pa WSS is predicted.

In combination, analysis indicates that a potential region in the CCA is at risk of atherosclerosis plaque formation. High OSI, elevated WSSAD and WSSAG, along with low WSS, WSSTG, WSSG values all signal towards this region along the outer wall. It should also be noted, that Vermeersch *et al* [9] found that within the CCA, the OSI provided a better statistical correlation to increased IMT than the WSSAG parameter. This, in concert with the high values of WSS, WSSG and WSSTG occurring near the apex, would indicate that the potential region of atherosclerosis predicted by WSSAD and WSSAG is misleading, and that the potential region predicted is a false positive.

Outside of the CCA, the indicators are less conclusive. Within the regions of low WSS, WSSG and WSSTG only elevated levels of OSI and low values of WSSAD and WSSAG occur. Therefore, the potential for atherogenesis outside the CCA is low.

As mentioned previously, results for the Wolverhampton dataset will also be presented, These geometries are derived from patients that have been clinically diagnosed with a stenosis within one of their carotid arteries. As such, plaque formation will already have occurred. It will allow an investigation into the understanding of the various stages of atherosclerosis and how the haemodynamic wall parameters alter to reflect each stage.

7 Conclusions

The right carotid bifurcation from Patient 1 has been investigated using six wall shear stress derived parameters. These parameters, in concert, indicate a region of potential atherosclerotic plaque formation. Near the flow divider, the peak time-averaged wall shear stress of 23Pa along with peak values for WSSTG and WSSG occur, indicating an athero-protective region. Although the results obtained depend on the patient-specific nature of the geometry, the results have been in good agreement with established literature. Further investigations will be presented on diseased carotid bifurcations.

REFERENCES

[1] D. N. Ku, D. P. Giddens, C. K. Zarins, and S. Glagov. Pulsatile flow and atherosclerosis in the human carotid bifurcation - positive correlation between plaque location and low and oscillating shear-stress. *Atherosclerosis*, 5(3):293–302, 1985.

[2] F. P. Glor, Q. Long, A. D. Hughes, A. D. Augst, B. Ariff, S. A. McG. Thom, P. R. Verdonck, and X. Y. Xu. Reproducibility study of magnetic resonance image-based computational fluid dynamics prediction of carotid bifurcation flow. *Annals of Biomedical Engineering*, 31:142–151, 2003.

[3] P. Papathanasopoulou, S. Zhao, U. Köhler, M. B. Robertson, Q. Long, and P. Hoskins. MRI measurement of time-resolved wall shear stress vectors in a carotid

bifurcation model, and comparison with CFD predictions. *Journal of Magnetic Resonance Imaging*, 17:153–162, 2003.

[4] K. T. Nguyen, C. D. Clark, T. J. Chancellor, and D. V. Papavassiliou. Carotid geometry effects on blood flow and on risk for vascular disease. *Journal of Biomechanics*, 41:11–19, 2008.

[5] J. Hwang, A. Saha, Y. C. Boo, G. P. Sorescu, J. S. McNally, S. M. Holland, S. Dikalov, D. P. Giddens, K. K. Griendling, D. G. Harrison, and H. Jo. Oscillatory shear stress stimulates endothelial production of from p47phox-dependent nad(p)h oxidases, leading to monocyte adhesion. *Journal of Biological Chemistry*, 278:47291–47298, 2003.

[6] T. Nagel, N. Resnick, C. F. Dewey Jr, and M. A. Gimbrone Jr. Vascular endothelial cells respond to spatial gradients in fluid shear stress by enhanced activation of transcription factors. *Arterisoscelerosis, Thrombosis, and Vascular Biology*, 19:1825–1834, 1999.

[7] B. C. Berk, J-I Abe, W. Min, J. Surapisitchat, and C. Yan. Endothelial atheroprotective and anti-inflammatory mechanisms. *Annals of New York Acadamy of Sciences*, 947:93–111, 2001.

[8] M. L. Bots, A. Hofman, Paulus T. V. M. De Jong, and D. E. Grobbee. Common carotid intima-media thickness as an indicator of atherosclerosis at other sites of the carotid artery the Rotterdam Study. *Annals of Epidemiology*, 6(2):147–153, 1996.

[9] S. J. Vermeersch, F. P. Glor, L. A. Crowe, B. Ariff, M. Bol, P. Segers, A. D. Hughes, X. Y. Xu, Thom SMcG, D. N. Firmin, and P. R. Verdonck. Relationship between carotid artery intima-media thickness and wall shear stress derived parameters. *Computer Methods in Biomechanics and Biomedical Engineering*, 8(4):279–280, 2005.

[10] S. Hyun, C. Kleinstreuer, P.W. Longest, and C.Chen. Particle-hemodynamics simulations and design options for surgical reconstruction of diseased carotid artery bifurcations. *Journal of Biomechanical Engineering*, 126:188–195, 2004.

[11] M. R. Kaazempur-Mofrad, A. G. Isasi, H. F. Younis, R. C. Chan, D. P. Hinton, G. Sukhova, G. M. LaMuraglia, R. T. Lee, and R. D. Kamm. Characterization of the atherosclerotic carotid bifurcation using MRI finite element modeling, and histology. *Annals of Biomedical Engineering*, 32:932–946, 2004.

[12] Mickaël Gay and Lucy T. Zhang. Numerical studies of blood flow in healthy, stenosed, and stented carotid arteries. *International Journal for Numerical Methods in Fluids*, 61:453–472, 2009.

[13] H. F. Younis, M. R. Kaazempur-Mofrad, R. C. Chan, A. G. Isasi, D. P. Hinton, A. H. Chau, L. A. Kim, and R. D. Kamm. Hemodynamics and wall mechanics in human carotid bifurcation and its consequences for atherogenesis - investigation of inter-individual variation. *Biomechanics and Modeling in Mechanobiology*, 3:17–32, 2004.

[14] P. Nithiarasu. A simple locally conservative Galerkin (LCG) finite element method for transient conservation equations. *Numerical Heat Transfer, Part B Fundamentals*, 46:357–370, 2004.

[15] C. G. Thomas. *A locally Conservative Galerkin (*LCG*) Method for convection-diffusion and Navier-Stokes equations*. PhD Thesis, Civil and Computational Engineering Centre, School of Engineering, Swansea University, 2006.

[16] C. G. Thomas and P. Nithiarasu. An element-wise, locally conservative Galerkin (LCG) method for diffusion and convection-diffusion problems. *International Journal for Numerical Methods in Engineering*, 73(5):642–664, 2008.

[17] C. G. Thomas, P. Nithiarasu, and R. L. T. Bevan. The locally conservative Galerkin (LCG) method for solving incompressible Navier-Stokes equations. *International Journal For Numerical Methods in Fluids*, 57:1771–1792, 2008.

[18] R.L.T. Bevan, P. Nithiarasu, R. Van Loon, I. Sazonov, H. Luckraz, and A. Garnham. Application of a locally conservative galerkin (lcg) method for modelling blood flow through a patient-specific carotid bifurcation. *International Journal for Numerical Methods in Fluids*, DOI: 10.1002/fld.2313.

[19] T. J. R. Hughes, G. Engel, L. Mazzei, and M. G. Larson. The continuous galerkin method is locally conservative. *Journal of Computational Physics*, 163:467–488, 2000.

[20] P. Nithiarasu. An efficient artificial compressibility (AC) scheme based on the charcteristic based split (CBS) method for incompressible flows. *International Journal for Numerical Methods in Engineering*, 56:1815–1845, 2003.

[21] O. C. Zienkiewicz, R. L. Taylor, and P. Nithiarasu. *The finite element method for fluid Dynamics*. Elsevier Butterworth Heinemann, London, 2005.

[22] P. Nithiarasu and O. C. Zienkiewicz. Analysis of an explicit and matrix free fractional step method for incompressible flows. *Computer Methods in Applied Mechanics and Engineering*, 195:5537 – 5551, 2006.

[23] O. C. Zienkiewicz and R. Codina. A general algorithm for compressible flow - part I. the split characteristic-based scheme. *International Journal for Numerical Methods in Fluids*, 20:869–885, 1995.

[24] O. C. Zienkiewicz, K. Morgan, B. V. K. S. Sai, R. Codina, and M. Vazquez. A general algorithm for compressible flow - part II. tests on the explicit form. *International Journal for Numerical Methods in Fluids*, 20:887–913, 1995.

[25] P. Nithiarasu, R. Codina, and O. C. Zienkiewicz. The characteristic based split scheme - a unified approach to fluid dynamics. *International Journal for Numerical Methods in Engineering*, 66:1514–1546, 2006.

[26] P. Nithiarasu. A matrix free fractional step method for static and dynamic incompressible solid mechanics. *Int. J. Comp. Meth. Eng. Sci and Mech.*, 7:369–380, 2006.

[27] P. Nithiarasu, J. S. Mathur, N. P. Weatherill, and K. Morgan. Three dimensional incompressible flow calculations using the characteristic based split (CBS) scheme. *International Journal for Numerical Methods in Fluids*, 44:1207–1229, 2004.

[28] P. H. Saksono, P. Nithiarasu, and I. Sazonov. Computational flow studies in a subject-specific human upper airway using one-equation turbulence model. influence of the nasal cavity. *Int. J. Numer. Meth. Engng*, Submitted 2010.

[29] N.P. Weatherill and O. Hassan. Efficient 3-dimensional delaunay triangulation with automatic point creation and imposed boundary constraints. *International Journal for Numerical Methods in Engineering*, 37(12):2005–2039, 1994.

[30] G. Karner, K. Perktold, M. Hofer, and D. Liepsch. Flow characteristics in an anatomically realistic compliant carotid artery bifurcation model. *Computer Methods in Biomechanics and Biomedical Engineering*, 2(3):171–185, 1998.

[31] A.D. Augst, B.Ariff, S.A.G. McG. Thom, X.Y.Xu, and A.D.Hughes. Analysis of complex flow and the relationship between blood pressure, wall shear stress and intima-media thickness in the human carotid artery. *Am J Physiol Heart Circ Physiol*, 293:1031–1037, 2007.

[32] T.E.Tezduyar, S. Sathe, T. Cragin, B. Nanna, B.S. Conklin, J. Pausewang, and M. Schwaab. Modelling of fluid-structure interactions with the space-time finite elements: Arterial fluid mechanics. *International Journal for the Numerical Methods in Fluids*, 54:901–922, 2007.

[33] S. E. Lee, S-W. Lee, P. F. Fischer, H. S. Bassiouny, and F. Loth. Direct numerical simulation of transitional flow in a stenosed carotid bifurcation. *Journal of Biomechanics*, 41:2551–2561, 2008.

[34] J. P. Mynard and P. Nithiarasu. A 1D arterial blood flow model incorporating ventricular pressure, aortic valve and regional coronary flow using the locally conservative galerkin (LCG) method. *Communications in Numerical Methods in Engineering*, 24:367–417, 2008.

[35] J.S. Milner, J.A. Moore, B.K. Rutt, and D.A. Steinman. Hemodynamics of human carotid artery bifurcations: Computational studies with models reconstructed from magnetic resonance imaging of normal subjects. *Journal of vascular surgery*, 28:143–156, 1998.

[36] I. Marshall, P. Papathanasopoulou, and K. Wartolowska. Carotid flow rates and flow division at the bifurcation in healthy volunteers. *Physiological Measurement*, 25:691–697, 2004.

[37] A.M. Malek, S.L. Alper, and S. Izumo. Hemodynamic shear stress and its role in atherosclerosis. *Journal of the American Medical Association*, 282:2035–2042, 1999.

[38] C. Cheng, D. Tempel, R van Haperen, A. van der Baan, F. Grosveld, M. Daemen, R. Krams, and R. de Crom. Atherosclerotic lesion size and vulnerability are determined by patterns of fluid shear stress. *Circulation*, 113:2744–2753, 2006.

[39] J. R. Buchanan, C. Kleinstreuer, S. Hyun, and G. A. Truskey. Hemodynamics simulation and identification of susceptible sites of atherosclerotic lesion formation in a model abdominal aorta. *Journal of Biomechanics*, 36:1185–1196, 2003.

[40] M. Lei, C. Kleinstreuer, and J.P. Archie Jr. Geometric design improvements for femoral graft-artery junctions mitigating restenosis. *Journal of Biomechanics*, 29:1605–1614, 1996.

[41] C. Kleinstreuer. *Biofluid Dynamics Principles and Selected Applications*. Taylor & Francis, 2006.

[42] X. He and D.N. Ku. Pulsatile flow in the human left coronary artery bifurcation: Average conditions. *Journal of Biomechanical Engineering*, 118:74–82, 1996.

[43] Y. Tardy, N. Resnick, T. Nagel, M. A. Gimbrone Jr, and C. F. Dewey Jr. Shear stress gradients remodel endothelial monolayers in vitro via a cell proliferation-migration-loss cycle. *Arteriosclerosis, Thrombosis, and Vascular Biology*, 17:3102–3106, 1997.